

Optical potentials for p -shell heavy ion projectiles

T. Yamaya, O. Satoh, and S. M. Morita*

Department of Physics, Tohoku University, Sendai 980, Japan

K. Kotajima and K. Hasegawa

Department of Nuclear Engineering, Tohoku University, Sendai 980, Japan

T. Shinozuka and M. Fujioka

Cyclotron and Radioisotope Center, Tohoku University, Sendai 980, Japan

(Received 8 February 1988)

Elastic and inelastic scatterings of ^{12}C , ^{13}C , ^{14}N , and ^{16}O projectiles on ^{28}Si have been studied at corresponding bombarding energies to the scattering in regions of the vicinity of the strong absorption radius. Optical model and microscopic double-folding model analyses have been performed in order to define the nature of the optical potential depending on the projectiles. The analysis by the optical model calculations showed that the shallow potential ($V_R = 10$ MeV) was not adequate for reproducing both the measured elastic and inelastic angular distributions, and a spin-dependent noncentral potential for the scattering systems $^{13}\text{C}, ^{14}\text{N} + ^{28}\text{Si}$ was indispensable for obtaining the similar central potentials for all four projectiles. Analysis by the microscopic double-folding calculations supported the results of the optical model calculations.

I. INTRODUCTION

In general, the majority of heavy ions elastic scattering at relatively low bombarding energies below 10 MeV per nucleon shows the characteristic Fresnel or Fraunhofer diffraction patterns in the angular distribution. The scattering under these circumstances is sensitive to the potential in the vicinity of the strong absorption radius.¹ Therefore, in such a radius, the observed cross sections are susceptible to a slight variation of the optical potential. For instance, the slope of the angular distributions imparts the information of the strong absorption radius and an exponentially decreasing oscillatory pattern gives the information about the potential in a region of the nuclear radius, where the nuclear forces begin to act inside the nuclear surface. The oscillatory pattern originates in an interference of waves diffracted from the far and near-side at the vicinity of the strong absorption radius, where the waves diffracted from the far-side enhances an effect of a short ranged attraction force at the nuclear surface. In such a surface region, the nuclear force may be so sensitive that one may perceive a somewhat weak surface-type potential, adding to the strong central potential. As the surface-type potential, a spin-orbit force arising from the valence nucleon(s) of the nucleus, is commonly thought. The spin-orbit potential for the heavy ion scattering is much weaker in proportion to $1/A_p^2$ than for the light ion scattering,^{2,3} where A_p is a projectile mass. However, the experimental evidence has been accumulating to indicate that a spin-dependent effect is much stronger for the transfer reaction.⁴⁻⁷ This effect of the optical potential, depending on the spin of the projectiles, is also expected to appear for the heavy ion scattering in the vicinity of the strong absorption radius.

In the present work, the elastic and inelastic scattering

of the p -shell nuclei ^{12}C , ^{13}C , ^{14}C , and ^{16}O projectiles on ^{28}Si have been studied as a case for the applicability of the projectiles dependence of the optical potentials. In the scattering system $^{16}\text{O} + ^{28}\text{Si}$, Cramer *et al.* and Satchler suggested that the elastic scattering data,^{8,9} at the bombarding energies between 33 and 215 MeV, are fitted by the optical potentials with a deep and energy-independent real part.¹⁰ This result shows that the non-locality for the real potential of heavy ions should be even less. Theoretically,¹¹ the reduced energy dependence of the heavy ion real potential can be derived from a folding model, decreasing as inverse proportion of a projectile mass. In the present investigation of the real potential, therefore, we assumed an energy independence of the optical model parameters at nearly equal bombarding energies of the projectiles.

II. EXPERIMENTAL PROCEDURE

The elastic and first excited state inelastic differential cross sections for the scattering of ^{12}C , ^{13}C , ^{14}N , and ^{16}O by ^{28}Si have been measured. The $^{12}\text{C}^{4+}$, $^{13}\text{C}^{4+}$, $^{14}\text{N}^{5+}$, and $^{16}\text{O}^{5+}$ ions^{12,13} were accelerated to the energies of 65, 60, 84, and 75 MeV, respectively, with the Tohoku University model-680 cyclotron. The target was a self-supporting natural Si metal, $180 \mu\text{g}/\text{cm}^2$ in thickness. The beam was doubly collimated to a $2 \times 4 \text{ mm}^2$ spot on the target. A counter system consists of two $25 \mu\text{m}$ totally depleted surface barrier type silicon detectors and a $240 \mu\text{m}$ position-sensitive silicon detector. Two ΔE detectors were placed in parallel with the position sensitive detector, i.e., this counter system has two telescopes $\Delta E_1 - E$ and $\Delta E_2 - E$. Each telescope was mounted by a tantalum plate with three slits in front of the ΔE detectors. Using this counter system, the spectra can be mea-

sured at six angles at the same time. The slit aperture of detector system is 2 mm wide and 8 mm high, and the solid angles are 1.7×10^{-4} – 2.2×10^{-4} sr. These solid angles depend on the position of the slit because of the geometrical condition in distance from the beam spot on the target. The overall angular resolution, including a beam emittance, have been determined by measuring the kinematically spread energy spectra of $^{14}\text{N}^{5+}$ ions elastically scattered from a thin ^9Be target. This results in an angular resolution of within 0.6° in the laboratory system. In the present experiment, for the purpose of observation of the exponentially decreasing oscillatory pattern in the angular distribution, the angular resolution, within at least 1° , is required for the measurements of differential cross section. The elastic and the inelastic differential scattering cross sections were measured at 65 MeV for ^{12}C , 60 MeV for ^{13}C , 84 MeV for ^{14}N , and 75 MeV for ^{16}O for angles 7° – 48° with steps of 0.7° – 1.0° in the laboratory system. Relative differential cross sections were normalized by the elastic scattering yield into a fixed monitor detector. Absolute cross sections were obtained by normalizing the elastic scattering yield to Rutherford cross sections at small angles, and by a determination of the target thickness from energy loss measurements with ^4He ions. The uncertainty in the absolute cross sections was estimated to be less than 5%.

III. EXPERIMENTAL RESULTS

Experimental elastic and first excited-state inelastic differential scattering cross sections are shown in Figs. 1(a) and (b), respectively, together with the distorted-wave Born approximation (DWBA) calculation curves. The differential cross sections at $E_{\text{lab}} = 75$ MeV for the scattering system $^{16}\text{O} + ^{28}\text{Si}$ are almost in agreement with the results of the data at $E_{\text{lab}} = 71$ MeV obtained by Cramer *et al.*⁹ However, the cross sections at forward angles measured by them drop exponentially without exhibiting oscillations because of angular distribution measurements with a large angular step. On the other hand, in the present experiment the oscillations coupled to the exponential decay were clearly observed at forward angles. Similarly, in the case of the scattering system, $^{14}\text{N} + ^{28}\text{Si}$ at $E_{\text{lab}} = 84$ MeV the present cross sections are in agreement with the data obtained by Kohono *et al.*,¹⁴ except for the oscillation pattern.

Figure 2 shows that the oscillation for the scattering system $^{14}\text{N} + ^{28}\text{Si}$ originates in waves diffracted from the near- and far-side in the strong absorption region where the short ranged attraction force begins to act at the nuclear surface. Theoretical curves are provided by decomposing the scattering amplitude into the near- and far-side components using a conventional six-parameter

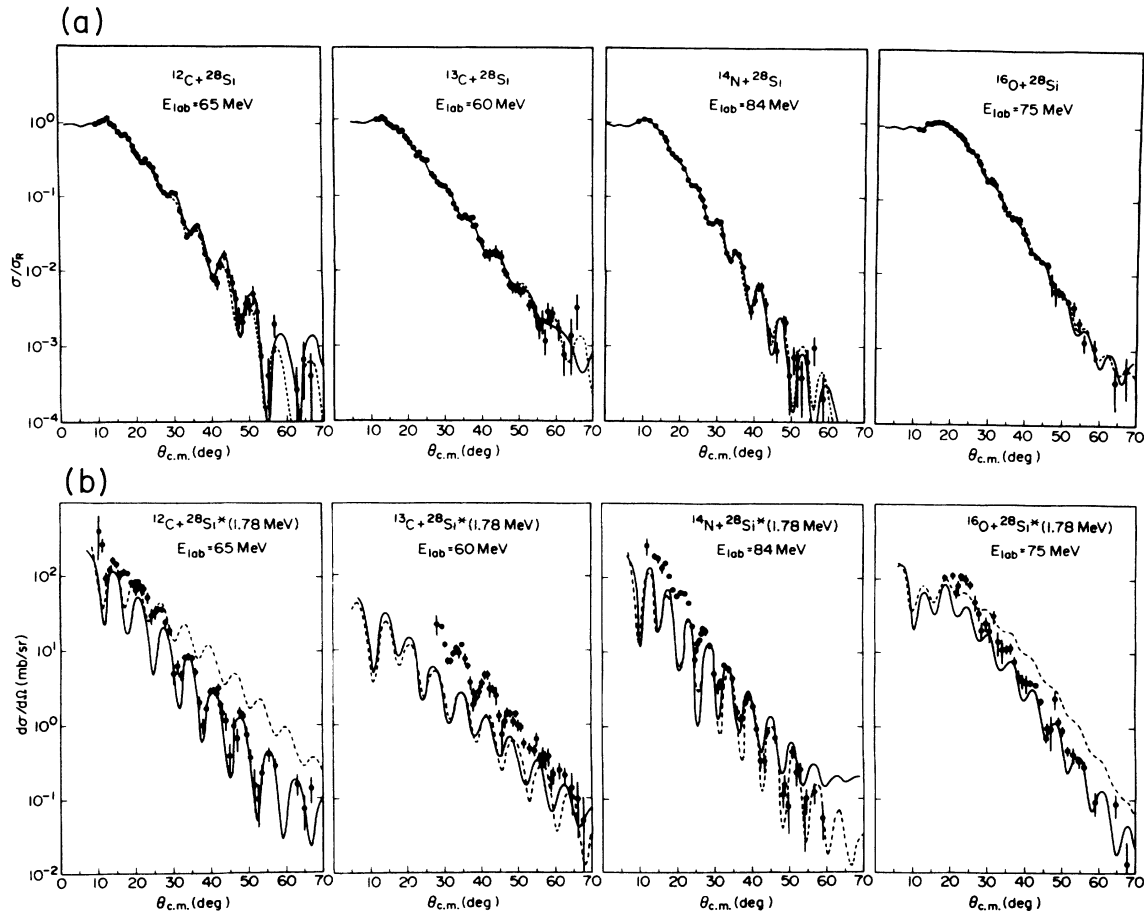


FIG. 1. Angular distributions of (a) elastic scattering and (b) inelastic scattering in the scattering systems ^{12}C , ^{13}C , ^{14}N , and $^{16}\text{O} + ^{28}\text{Si}$. The solid and the dotted curves are the best fit to the data by the optical potential calculations with the deep and shallow potentials, respectively. The parameters obtained from these fitting are listed in Table II.

Woods-Saxon well potential. The dotted curve in Fig. 2 indicates the cross sections by the near-side scattering amplitude. This angular distribution drops exponentially without exhibiting oscillations. The dashed curve indicates the cross section by the far-side scattering amplitude. The far-side differential cross section at $\theta_{c.m.} = 30^\circ$ is about 2 orders smaller than the near-side cross section. Nevertheless, as shown by the solid curve, the oscillation originated in an interference between the near- and far-side amplitudes appeared explicitly in the angular distribution reproducing the present data. Similar results were obtained for other projectiles in the present measurement.

IV. ANALYSIS

A. Optical model potentials

One of the potentials studied by Cramer *et al.*,⁹ called by them *A*-23, had a depth fixed at $V = 100$ MeV. This potential gave a distinctly poorer fit to the data by Cramer *et al.* than their shallow potential called *E*-18, which had $V = 10$ MeV. Satchler¹⁰ reanalyzed the data⁹ using the corresponding parameter values, allowing the diffuseness of the imaginary potential depending on the bombarding energy. This immediately allowed a good fit to the data at the bombarding energies between 33 and 215 MeV, comparable to that obtained with the shallow potential, with the parameter values called the *A* type.

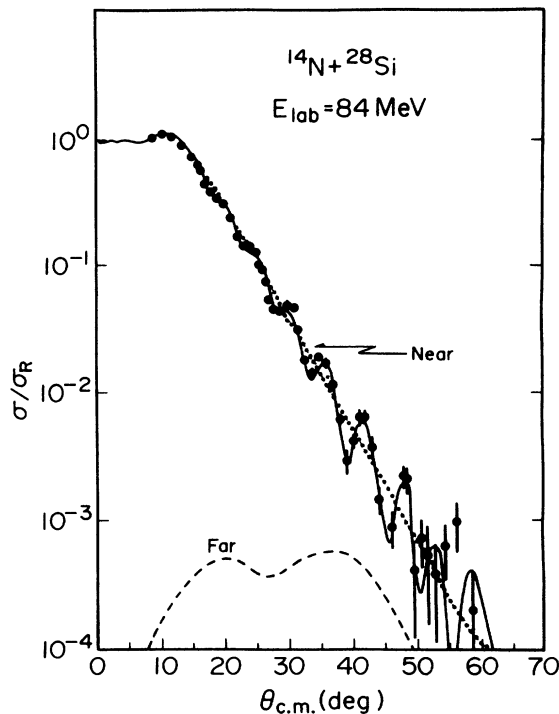


FIG. 2. The oscillation pattern of the elastic scattering in the system $^{14}\text{N} + ^{28}\text{Si}$ at the bombarding energy of 84 MeV. The dotted curve indicates the cross section from the near-side diffraction and the dashed curve indicates the cross section from the far-side diffraction. The solid curve is a coherent sum of these.

In the present analyses, the elastic and inelastic scattering cross sections were fitted using an optical model potential of Woods-Saxon type. The optical model calculation was made using the computer codes ELAST2,¹⁵ ALPS,¹⁶ and CHUCK.¹⁷ At first, we analyzed the present data in the scattering system $^{16}\text{O} + ^{28}\text{Si}$ using the optical potential parameters obtained from the deep potential of *A* type by Satchler,¹⁰ and the shallow potential of *E*-18 by Cramer *et al.*⁹ The results of the calculations were compared with the measured cross sections in Figs. 3(a) and (b). The dashed curves indicate the results of the calculations with the deep potential *A* type in Fig. 3(a) and with the shallow potential *E*-18 in Fig. 3(b). These potentials could not reproduce the oscillations in the measured angular distribution and seem to reproduce only the near-side scattering cross section (see Fig. 2). We tried to search other potential parameters to fit into the present data. The real well depths were fixed at 100 MeV as a deep potential and 10 MeV as a shallow potential, where the radius parameter of the imaginary potential r_I was also fixed at 1.073 fm of the *A* type for the deep potential parameter search. The results are indicated by the solid curves in Figs. 3(a) and (b), reproducing the measured cross section. The resulting optical potential parameters are compared with those of Cramer *et al.*, and of Satchler in Table I. It is shown in χ^2/N values that the fit to the data tends to be similar for the shallow and the deep potentials. As a consequence of the above analysis, the optical model parameters were newly searched for all four projectiles on ^{28}Si to reproduce the oscillation in the angular distributions. As the first step of the optical potential search, a conventional six-parameter Woods-Saxon potential was used. In the deep potential parameter search, the real well depths were grided on from $V_R = 60$ to 100 MeV in steps of 2 MeV and all of the remaining five parameters were free. The real well depth of the shallow potential was fixed at 10 MeV, which is the same as the *E*-18, and the other parameters were also free. For the parameters of ^{13}C and ^{14}N projectiles, good fit to the elastic data were impossible unless $V_R \geq 30$ MeV. The best fit curves are compared with the elastic scattering data in Fig. 1(a). The calculation curves with the deep and shallow potentials are indicated by the solid and dashed curves, respectively. The used potential parameters are listed together with the minimum values of χ^2/N in Fig. 2.

The phenomenological optical potentials that give the optimum fits to elastic scattering data are available to evaluate the predictions of various nuclear structure model by a comparison with inelastic scattering data.¹⁸ For the deformed nucleus, such as ^{28}Si , the usual prescription is to take a nonspherical surface, and the spherical part is identified with the empirical optical potential deduced from the elastic scattering data. An effective interaction in the distorted wave Born approximation calculation is deduced from a slope of this potential, and the angular distribution of the inelastic scattering is determined for a given angular momentum transfer L . Thus, this means some examination of the optical potential, deduced from the elastic scattering data of the DWBA calculation with its optical potential, reproduces

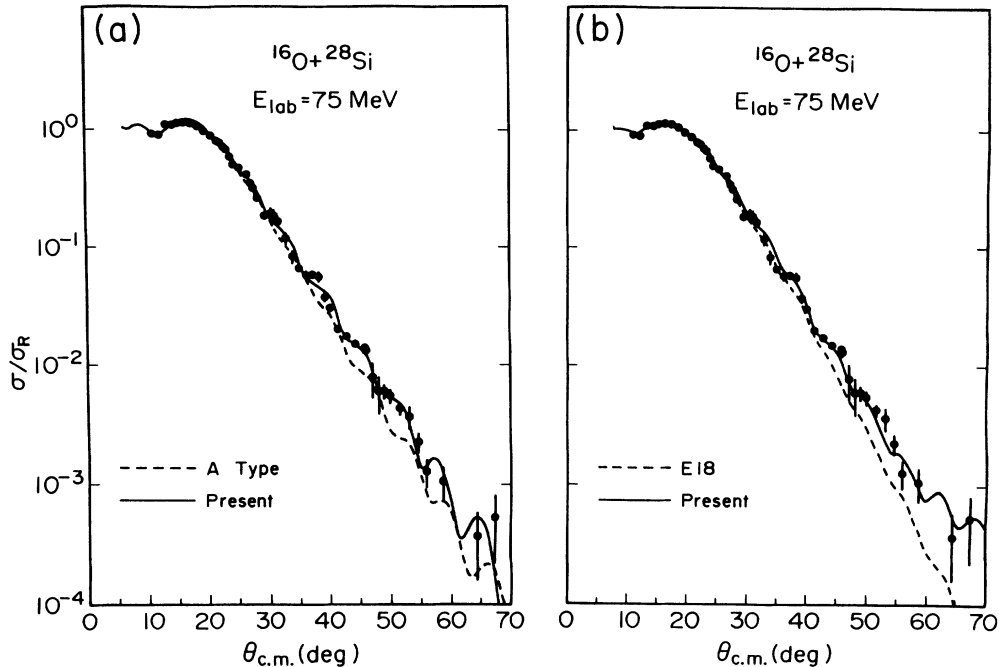


FIG. 3. Comparison between the optical model calculations using the present parameters (solid curves), the parameters of *A* type [dashed curve in (a)], and of *E-18* [dashed curve in (b)] for scattering system $^{16}\text{O} + ^{28}\text{Si}$ at 75 MeV.

the inelastic scattering data. The results of the calculations for the inelastic scattering system ^{12}C , ^{13}C , ^{14}N , and $^{16}\text{O} + ^{28}\text{Si}^*$ (1.78 MeV, 2^+) are shown in Fig. 1(b). The used optical potential parameters were those listed in Table II. The ^{28}Si was assumed to be an axially symmetric $R = R_0(1 + \beta_2 Y_{20})$, where β_2 represents the quadrupole deformation parameter of the ^{28}Si . The Coulomb excitation effect was explicitly included. The value of $\beta_2^N = \beta_2^C = -0.274$ was adopted for the 1.78 MeV 2^+ first excited state of ^{28}Si , where notations *N* and *C* indicate the nuclear and the Coulomb parts, respectively. This value was deduced from the inelastic scattering data of ^{16}O on $^{28}\text{Si}^*$ at 56 MeV by Mermaz *et al.*¹⁹ In Fig. 1(b), the solid and dashed curves indicate the results of the DWBA calculations with the deep and shallow potentials, respectively, and are listed in Table II. For ^{12}C and ^{16}O , the solid curves reproduced the data well, but the dashed curves could not reproduce the data. It was impossible to fit the dashed curves to the inelastic data by a small variation of the optical parameters. This discrepancy between the theoretical and experimental

cross sections is caused by the effective interaction deduced from the small real well depth of 10 MeV in the shallow potential. This result suggests that a realistic effective interaction for inelastic scattering should be deduced from a deep potential, which resembles a folded potential. For the projectiles ^{13}C and ^{14}N , those theoretical curves obtained using the deep potential show a similar diffraction pattern, however, these could not reproduce the inelastic data as well as in the case for ^{12}C and ^{16}O . Thus, the optical potentials for ^{13}C and ^{14}N should be corrected by somewhat other potentials, other than the central potentials.

The ^{28}Si nucleus is known to be a strongly deformed rotational nucleus with an oblate deformation. Thus, in the analysis, by means of a coupled-channel code, we attempted to fit the inelastic cross sections simultaneously with the elastic cross sections for the scattering systems $^{13}\text{C} + ^{28}\text{Si}$ and $^{14}\text{N} + ^{28}\text{Si}$, using the computer code CHUCK3.¹⁷ The quadrupole deformation parameter β_2 of the first excited state of ^{28}Si was the same value used in the analysis of the inelastic data. The results of the

TABLE I. Parameters of optical model potentials. In this table $R = r_0 (A_p^{1/3} + A_T^{1/3})$ and $r_{\text{Coul}} = 1.0$ fm.

Potential	V_R (MeV)	r_R (fm)	a_R (fm)	W_I (MeV)	r_I (fm)	a_I (fm)	χ^2/N
<i>E-18</i> ^a	10	1.35	0.681	23.4	1.23	0.552	12.5
Present	10	1.38	0.456	41.8	1.13	0.575	6.1
<i>A</i> type ^b	100	0.969	0.745	44.1	1.073	0.605	15.4
Present	100	1.059	0.610	35.7	1.073	0.671	6.8

^aCramer *et al.* (Ref. 3).

^bSatchler (Ref. 4).

TABLE II. Optical potential parameters fitted to the data. The imaginary potential W is of a volume type. The geometric radius parameter was defined in $R = r_0 (A_P^{1/3} + A_T^{1/3})$.

Potential	E_{lab} (MeV)	V_R (MeV)	r_R (fm)	a_R (fm)	W_I (MeV)	r_I (fm)	a_I (fm)	χ^2/N
^{12}C	65							
Shallow		10.0	1.38	0.484	24.67	1.25	0.413	6.40
Deep		88.0	1.08	0.596	43.86	1.04	0.641	9.23
^{13}C	60							
Shallow		30.0	1.23	0.466	23.40	1.01	1.069	3.50
Deep		74.0	1.17	0.458	12.37	1.14	1.067	3.18
^{14}N	84							
Shallow		30.0	1.23	0.522	41.84	1.00	0.843	7.84
Deep		70.0	1.15	0.527	10.08	1.20	0.920	6.29
^{16}O	75							
Shallow		10.0	1.38	0.456	41.84	1.13	0.575	6.13
Deep		90.0	1.07	0.621	31.07	1.12	0.635	7.04

coupled-channel calculations are indicated by the dashed curves in Figs. 4(a) and (b) for the elastic and the inelastic data, respectively, in order to understand the effects of the channel coupling to the excited state of ^{28}Si . The results of this analysis indicated that a simultaneous fit to

both the elastic and inelastic data could not be found by the coupled-channel calculations for the parameter search on the basis of the deep potentials in Table II.

In the next step of fitting the elastic cross sections simultaneously with the inelastic cross sections for the

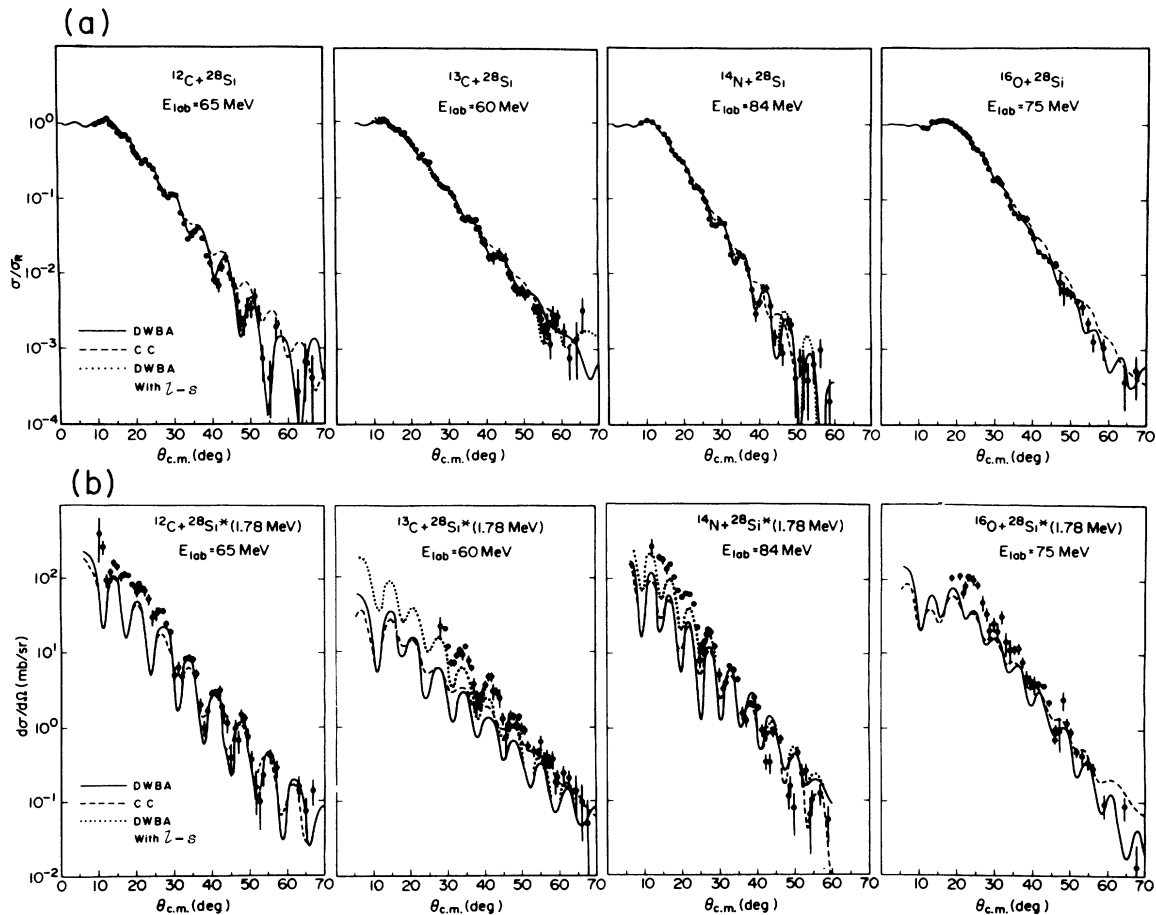


FIG. 4. Various calculations fits to (a) elastic and (b) inelastic scattering data. The solid, dashed, and dotted curves indicate the results of the calculations with the deep potential, coupled-channel, and deep + $1-s$ parameters, respectively.

projectiles ^{13}C and ^{14}N , the optical potential parameters were searched for the nine-parameter Woods-Saxon potential, including a spin-orbit term. In the spin-orbit potential for the heavy ion collision, there is little experimental information. According to a single-folding method, the mass number dependence of the spin-orbit potential obtained is almost proportional to $1/A_p^2$, i.e., inversely proportional to the square of the nuclear volume. In the present scattering systems, the spin-orbit potentials of ^{13}C and ^{14}N were derived from the empirical proton and deuteron spin-orbit potentials for ^{28}Si , respectively, using the single-folding model.^{2,3} The preliminary values of the calculated spin-orbit potential depth were 0.05 and 0.1 MeV for ^{13}C and ^{14}N projectiles, respectively. In the present analysis, however, the standard Thomas shape was adopted as an “effective spin-orbit potential.” The central real well depth of the deep potentials were grided on from $V_R=60$ to 100 MeV in steps of 2 MeV, and all of the remaining eight parameters were free for the elastic cross sections. The resulting parameters are given in Table III together with the minimum values of χ^2/N and the calculation curves corresponding to these minimum values were indicated by the dotted curves in Fig. 4(a). The inelastic scattering cross sections were also calculated using the parameters listed in Table III. The results of the calculation are indicated by the dotted curves in Fig. 4(b). These curves reproduce well the inelastic scattering data of the projectiles ^{13}C and ^{14}N .

B. Double folded potential

So far we have discussed the general characteristics of the optical model potential, which can account for the elastic and inelastic scattering. However, it is important to speculate about the characteristics of the projectiles in the scattering potentials. For the strongly deformed projectiles such as ^{12}C , in particular, the analysis, by means of a microscopic double-folding calculation, should be significantly performed. The real potentials in the calculation were obtained by folding an effective nucleon-nucleon interaction V_{NN} into the density distributions of the projectiles and the target ^{28}Si . The projectile and target nucleon densities were constructed from the wave functions, which give charge densities in agreement with electron scattering measurements. The double-folding calculations have been accomplished using a microscopic double-folding code.²⁰ As for the effective nucleon-nucleon interaction V_{NN} , the spin- and isospin-singlet ($S=T=0$) component of the $M3Y$ interaction was used.

This part is

$$V_{\text{NN}}(\mathbf{r}) = \left[7999 \frac{e^{-4r}}{4r} - 2134 \frac{e^{-2.5r}}{2.5r} - 262 \cdot \delta(\mathbf{r}) \right] \text{ MeV} .$$

The detailed parameters in the calculation have been described in a report by Sakuragi *et al.*²¹ The ground-state nucleon densities of ^{13}C , ^{14}N , and ^{28}Si are obtained from the charge densities with the electron scattering measurement,^{22,23} and the Hartree-Fock density²⁴ was employed for ^{16}O . As for ^{12}C , the density calculated with the microscopic $3\text{-}\alpha\text{RGM}$ wave function²⁵ was adopted. For the imaginary potentials a phenomenological Woods-Saxon shape was used. The shape of the real potential was determined by the folding procedure, but its strength was allowed to be renormalized by a scaling factor N_R . The results of the calculations were compared with the measured elastic cross sections in Fig. 5. The values of χ^2/N for the best fit to the data are listed in Table IV, together with the corresponding optical model parameters of the imaginary potential and the scaling factor N_R . The results of calculations with only the central potentials made a clear distinction of the potentials between the projectiles ^{12}C and ^{16}O , and the projectiles ^{13}C and ^{14}N for fit to the data. The potentials for ^{12}C and ^{16}O have the N_R of about 0.8 with the deep imaginary potential depth, and those for ^{13}C and ^{14}N have the N_R of about 1.0 with the shallow imaginary potential depth. On the other hand, the calculations with the potentials including the spin-orbit term, which has the Thomas shape as a noncentral spin-dependent potential, were performed for ^{13}C and ^{14}N to reproduce the elastic data. The results are indicated by the dotted curves in Fig. 5, and the obtained parameters are listed in Table IV. As seen in this table, the central potentials obtained from the calculations, including the spin-orbit term, approach those of the spinless projectiles ^{12}C and ^{16}O , that is, the scaling factor N_R of about 0.8 with the deep imaginary potentials.

V. DISCUSSION

The present work indicates that the scattering of the p -shell nuclei at energies about three times above the Coulomb barrier is sensitive to the nuclear surface features, depending on the spin. In the present analysis the spin-dependent potential is described as the “effective spin-orbit potential” in the phenomenological distorted wave and the microscopic double-folding calculations.

The six-adjustable parameters of the phenomenological

TABLE III. Optical potential parameters including a spin-orbit term fitted to the elastic and the inelastic data. The geometric radius parameter was defined in $R = r_0(A_p^{1/3} + A_T^{1/3})$.

Ions	V_R (MeV)	r_R (fm)	a_R (fm)	W_I (MeV)	r_I (fm)	a_I (fm)	$V_{\text{s.o.}}$ (MeV)	$r_{\text{s.o.}}$ (fm)	$a_{\text{s.o.}}$ (fm)	χ^2/N
^{13}C	84.0	1.08	0.642	46.14	0.963	0.800	-0.276	1.75	0.625	9.01
^{14}N	88.0	1.07	0.665	41.07	1.060	0.665	0.162	1.78	0.679	10.80

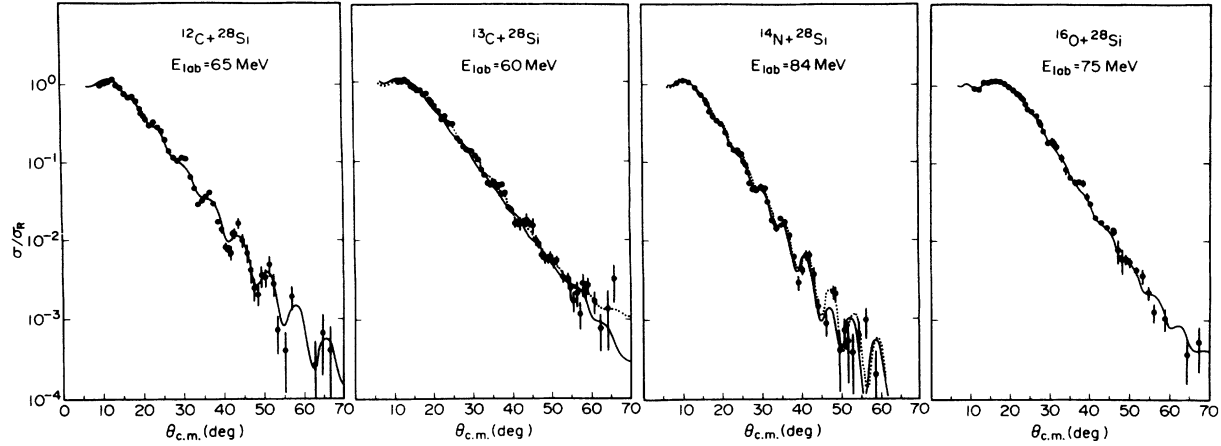


FIG. 5. Double-folding calculation fit to the elastic scattering data. The solid and dotted curves indicate the results of the calculation with and without the Thomas-shape spin-orbit term, respectively.

optical potential obtained from the best fit to the elastic scattering data are listed in Table II. Our investigations of the potential parameters are restricted to only the deep potential, because the shallow potentials obtained from the elastic data did not reproduce the inelastic data to the first excited state of ^{28}Si for all four projectiles. As listed in Table II, the optical potential parameters for the scattering systems $^{12}\text{C}+^{28}\text{Si}$ and $^{16}\text{O}+^{28}\text{Si}$ are nearly equal, in spite of the difference between the nuclear structures of ^{12}C and ^{16}O in the shell model. That is, an outer $1p_{1/2}$ orbit of ^{16}O is fully occupied with four nucleons but this orbit is empty for ^{12}C . This difference of structure between ^{12}C and ^{16}O was not clearly found in the optical potential parameters in the present analysis. The optical potentials in the scattering system $^{13}\text{C}+^{28}\text{Si}$ and $^{14}\text{N}+^{28}\text{Si}$ are also nearly equal. The outer $1p_{1/2}$ orbit of these projectiles is occupied with a neutron and with a neutron-proton pair coupled to the spin 1 for ^{13}C and ^{14}N nuclei, respectively. The clear difference between the spinless projectiles (^{12}C and ^{16}O) and the projectiles with spin (^{13}C and ^{14}N) was found in the central potential parameters by the analysis with the six-adjustable parameters. These optical potentials obtained from the elastic data were examined with the analysis in the inelastic scattering process to the first excited state of ^{28}Si , i.e., the DWBA calculations were made on the basis of the optical potential parameters of Table II. As seen from Fig. 1(b) the optical potentials for the projectiles of ^{12}C and ^{16}O

reproduced well the inelastic cross section but those of ^{13}C and ^{14}N poorly reproduced the data [see the solid and dashed curves in Fig. 1(b)]. These poor reproductions are caused by the inadequate real central potentials from which the effective interaction used in the inelastic scattering calculations are deduced. In the analysis with a nine-adjustable parameter for the elastic scattering data of ^{13}C and ^{14}N , a spin-orbit term of the Thomas shape was also introduced in the calculations as the “effective spin-orbit potential” [see Table III and Figs. 4(a) and (b)]. It is a consequence of introducing the spin-orbit term to the optical potentials that the real and imaginary central potentials of all four projectiles are nearly equal for the elastic scattering data. From this result the calculated inelastic cross sections reproduced the data in the scattering system $^{13}\text{C}+^{28}\text{Si}^*$ and $^{14}\text{N}+^{28}\text{Si}^*$ [see the dotted curves in Fig. 4(b)]. On the other hand, it was found that the effect of a coupling between the ground and first excited state of ^{28}Si was small in the coupled channel calculation for reproducing the inelastic data [the dashed curves in Fig. 4(b)].

Usual, strongly absorbing heavy ion optical potentials which yield good fit to low energy data have a central imaginary well depth of $\frac{1}{2}-\frac{1}{4}$ of a real depth.²⁶ In the scattering system $^{16}\text{O}+^{28}\text{Si}$ at the bombarding energies for 33 and 215 MeV,⁹ the good fit to the data showed a value of W_0/V_0 of about $\frac{1}{2}$ of the deep 100 MeV real potential.¹⁰ The ratios of the W_0/V_0 and the $W_{1/2}/V_{1/2}$ in

TABLE IV. Optical potential parameters in the double-folding calculations. Charge radius is $r_c = 1.0$ fm.

Ions	N_R	W_I (MeV)	r_I (fm)	a_I (fm)	$V_{s.o.}$ (MeV)	$r_{s.o.}$ (fm)	$a_{s.o.}$ (fm)	χ^2/N
^{12}C	0.74	43.90	1.12	0.55				8.6
^{13}C	1.0	17.25	1.26	0.73				6.9
(with 1-s)	0.74	66.28	0.97	0.87	-0.78	1.40	0.32	4.9
^{14}N	0.97	12.06	1.28	0.65				9.7
(with 1-s)	0.87	63.62	0.93	0.83	0.32	1.30	0.52	11.2
^{16}O	0.80	59.31	1.15	0.49				8.8

the present work are plotted in Fig. 6, where $V_{1/2}(W_{1/2})$ indicate the depth of the real (imaginary) potential at the strong absorption radius $R_{1/2}$. Both ratios of W/V at $R=0$ and at $R_{1/2}$ were almost $\frac{1}{2}$ for ^{12}C and ^{16}O projectiles. For ^{13}C and ^{14}N , the ratio of W/V obtained from the analysis with the six-adjustable parameters (excluding the spin-orbit term) resulted in very small values at $R=0$, but very large values at $R_{1/2}$. As the result of the analysis with the nine-adjustable parameters (including the spin-orbit term), however, the same ratios W/V of about $\frac{1}{2}$ at $R=0$ and $R_{1/2}$ were obtained for all four projectiles (see Fig. 6). That is, it was apparent by an introduction of the spin-dependent noncentral potential that the ratios of W/V keep a good balance in the nearly equal central potential for all four projectiles of the $1p_{1/2}$ shell nuclei.

At any one bombarding energy the scattering cross section is sensitive to contributions from only a few partial waves depended on the bombarding energy. Furthermore, the heavy ion potential could well be l dependent. Reflection coefficients for the deep potential sets in Table II are illustrated for each projectiles in Fig. 7. In the present case, as seen from Fig. 7, seven partial waves for ^{12}C and ^{16}O , ten partial waves for ^{14}N , and 13 partial waves for ^{13}C are contributed to the reflection coefficients

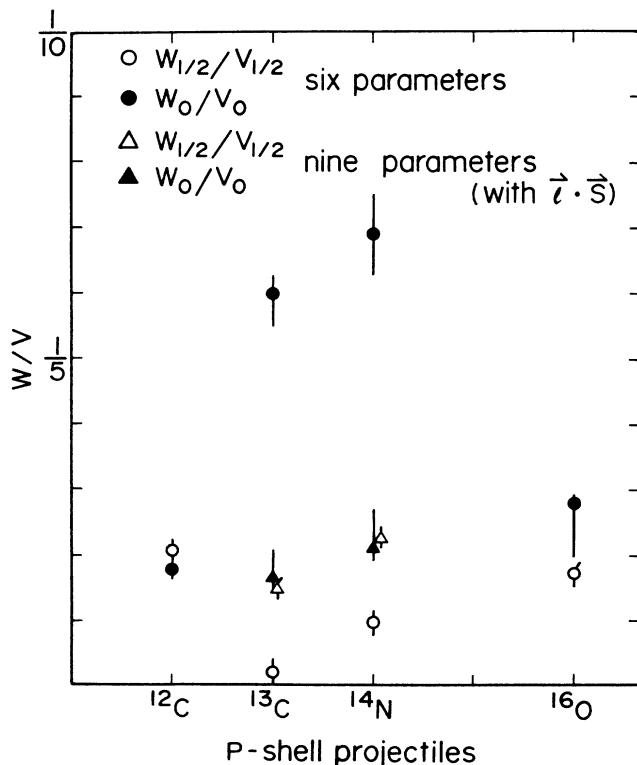


FIG. 6. Ratios of the imaginary potential depth to the real potential depth at the nuclear center $R=0$ (W_0/V_0) and at the strong absorption radius $R_{1/2}$ ($W_{1/2}/V_{1/2}$). The circles and triangles indicate the results calculated with the six-adjustable parameters and the nine-adjustable parameters (including the spin-orbit term), respectively. The vertical bars indicate regions of W/V values obtained from parameters fitted to the data within a 5% increase in the χ^2/N minimum values.

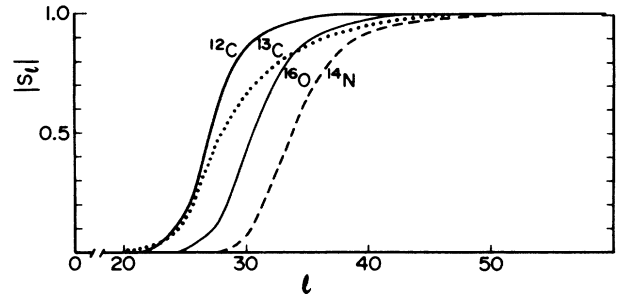


FIG. 7. Reflection coefficients for the scattering systems ^{12}C , ^{13}C , ^{14}N , and $^{16}\text{O}+^{28}\text{Si}$ calculated with the deep potential set of Table II. The bombarding energies are 65, 60, 84, and 75 MeV for the projectiles ^{12}C , ^{13}C , ^{14}N , and ^{16}O , respectively.

for $|S_l|^2=0.1-0.9$. It is noted that the numbers of partial waves of the ^{13}C and ^{14}N contributing to the scattering cross sections are more than those of the spinless projectiles ^{12}C and ^{16}O . In fact, at the strong absorption angular momentum $l_{1/2}$ taken at $|S_l|^2=\frac{1}{2}$, the partial waves of only $j_{1/2}=l_{1/2}$ contribute to $|S_l|^2=\frac{1}{2}$ for ^{12}C and ^{16}O projectiles. However, the partial waves of $l_{1/2}$ and $l_{1/2}\pm 1$ for ^{14}N and $l_{1/2}\pm\frac{1}{2}$ for ^{13}C are possible to contribute to $|S_l|^2=\frac{1}{2}$.

In a discussion of the scattering potential between the complex nuclei, the effect of the characteristics of the projectiles and target nuclei in the potential should be examined. The examination was made by the analysis using the microscopic double-folding calculations.^{16,20,21} The results obtained from the analysis are shown in Table IV and Fig. 5. The characteristics of the projectiles and target nuclei were reflected on these nucleon density distributions used in the double-folding calculations. These nucleon densities were constructed from the wave functions which give charge densities in agreement with electron scattering measurements. In the scattering system $^{16}\text{O}+^{28}\text{Si}$ the scaling factor of the double-folding potential $N_R=0.89$ and the imaginary central depth $W_I=90$ MeV, given in Ref. 10, did not reproduce the oscillatory pattern of the present data. The values of N_R and the W_I obtained from the present analysis are nearly equal for the scattering systems $^{12}\text{C}+^{28}\text{Si}$ and $^{16}\text{O}+^{28}\text{Si}$, i.e., $N_R=0.74$, $W_I=43.9$ MeV for ^{12}C , and $N_R=0.8$, $W_I=59.3$ MeV for ^{16}O projectiles. On the other hand, the values of $N_R=1.0$, $W_I=17.25$ MeV and $N_R=0.97$, $W_I=12.06$ MeV were obtained for the scattering systems $^{13}\text{C}+^{28}\text{Si}$ and $^{14}\text{N}+^{28}\text{Si}$, respectively. In the double-folding calculations for the scattering system $^{13}\text{C}+^{28}\text{Si}$ and $^{14}\text{N}+^{28}\text{Si}$, a spin-orbit potential of the Thomas shape were added to the central potentials as the "effective spin-orbit potential." The analysis with this calculation results in $N_R=0.74$, $W_I=66.28$ MeV, and $N_R=0.87$, $W_I=63.62$ MeV for ^{13}C and ^{14}N projectiles, respectively. It is a consequence of the analysis using the double-folding calculations that the scaling factor $N_R=0.74-0.87$ and the imaginary potential depth $W_I=44-66$ MeV are obtained for all four p -shell projectiles. This result is qualitatively in agreement with that of the analyses using the phenomenological optical model

calculations.

An effect of the microscopic coupled-channel among the ground state, the 2_1^+ and 3_1^- states of the ^{12}C projectile was preliminarily examined for the scattering system $^{12}\text{C}+^{28}\text{Si}$. The imaginary part of the coupling potential was switched off in the coupled-channel calculation. The calculations have been done using a microscopic coupled-channels code.²⁷ The result of the calculation reproduced the elastic scattering data with a small improvement of N_R to 0.8 from 0.74. However, the result of the calculation to the excited 2_1^+ state of ^{12}C did not reproduce the data of the scattering $^{12}\text{C}+^{28}\text{Si} \rightarrow ^{12}\text{C}(2_1^+)+^{28}\text{Si}$.

VI. SUMMARY AND CONCLUSIONS

The optical potentials in the scattering system ^{12}C , ^{13}C , ^{14}N , and $^{16}\text{O}+^{28}\text{Si}$ have been investigated at the nuclear radius allowing a transparent region near the nuclear surface but retaining strong absorption in the nuclear interior. In the vicinity of this nuclear radius, the shallow potential such a $V_R=10$ MeV was not adequate to reproduce both the elastic and inelastic scattering data because of the unrealistic effective interaction deduced from the shallow potential for the elastic scattering.

It became evident, in the analyses of the phenomenological optical potential calculations, that a noncentral potential depending on the spin was indispensable for the

reproduction of both the elastic and inelastic scattering data of the projectiles with spin, i.e., ^{13}C and ^{14}N . By introducing the Thomas-shape spin-orbit potential as an "effective spin-orbit potential," the optical potential with the similar real central and imaginary central potentials for all four projectiles of *1p*-shell nuclei were obtained from fit to both the elastic and inelastic scattering data.

A necessity of the spin-orbit term in the scattering system ^{13}C and $^{14}\text{N}+^{28}\text{Si}$ was confirmed by the analyses using the microscopic double-folding calculations. In this calculations the scaling factor N_R of the double-folding real central potential was about 0.8. An effect of the channel coupling to the excited states of the ^{12}C projectile that was calculated with the microscopic coupled-channel method was only about 10% increase in $N_R=0.74$ in the scattering system $^{12}\text{C}+^{28}\text{Si}$.

For the examination of the spin-dependent noncentral potential, it is expected to observe directly the polarization of scattered projectiles.

ACKNOWLEDGMENTS

The authors would like to thank Dr. Y. Sakuragi for his assistance in using the microscopic double-folding code and the microscopic coupled-channel code, and for valuable discussions. The authors wish to thank Dr. Y. Iseri for use of his program code, automatic search for optical potential parameter (ALPS).

*Present address: Mitsui Mining and Smelting Co., Ltd., Ageo, Saitama 362, Japan.

¹G. R. Satchler, Nucl. Phys. **A409**, 3C (1983).

²H. Amakawa and K.-I. Kubo, Nucl. Phys. **A266**, 521 (1976).

³W. J. Thompson, in *Proceedings of the International Conference on Reactions Between Complex Nuclei, Nashville, 1974*, edited by R. L. Robinson, F. K. McGowan, J. B. Ball, and J. H. Hamilton (North-Holland, Amsterdam, 1974), Vol. 1, p. 14.

⁴W. von Oertzen, E. R. Flynn, J. C. Peng, J. W. Sunier, and R. E. Brown, Z. Phys. A **301**, 365 (1981).

⁵S. Kubono, D. Dehnhard, D. A. Lewis, T. K. Li, J. L. Artz, D. J. Weber, P. J. Ellis, and A. Dudek-Ellis, Phys. Rev. Lett. **38**, 817 (1977).

⁶B. F. Bayman, A. Dudek-Ellis, and P. J. Ellis, Nucl. Phys. **A301**, 141 (1978).

⁷P. Wust, W. von Oertzen, H. Ossenbrink, H. Letau, H. G. Bohlen, W. Saathaff, and C. H. Wiedner, Z. Phys. A **291**, 151 (1979).

⁸D. S. Gale and J. S. Eck, Phys. Rev. C **7**, 1950 (1973).

⁹J. G. Cramer, R. M. DeVries, D. A. Goldberg, M. S. Zisman, and C. F. Maquire, Phys. Rev. C **14**, 2158 (1976).

¹⁰G. R. Satchler, Nucl. Phys. **A279**, 493 (1977).

¹¹D. F. Jackson and R. C. Johnson, Phys. Lett. **49B**, 249 (1974).

¹²T. Yamaya, K. Kotajima, T. Shinozuka, M. Fujioka, U. Sakurada, T. Onodera, T. Ishimat, and S. Morita, Nucl. Instrum. Methods **203**, 7 (1982).

¹³T. Yamaya, T. Shinozuka, K. Kotajima, M. Fujioka, and T. Onodera, Nucl. Instrum. Methods **226**, (1984).

¹⁴I. Kohono, S. Nakajima, T. Tonuma, and M. Odera J. Phys. Soc. Jpn. **30**, 910 (1971).

¹⁵M. Igarashi, Institute for Nuclear Study, University of Tokyo Report No. PT-26, 1970.

¹⁶Y. Iseri (unpublished).

¹⁷D. Kuntz, University of Colorado report, code CHUCK (unpublished), modified by J. R. Comfort.

¹⁸G. R. Satchler, *Direct Nuclear Reactions* (Oxford University Press, New York, 1983).

¹⁹M. C. Mermaz, M. A. G. Fernandes, A. Greiner, B. T. Kim, and N. Lisboa, Phys. Rev. C **19**, 794 (1979).

²⁰Y. Sakuragi, M. Yahiro, and M. Kamiura, Prog. Theor. Phys. Suppl. **89** (1986), Chap. VI; Y. Sakuragi, private communication.

²¹Y. Sakuragi, M. Yahiro, and M. Kamimura, Institute for Nuclear Study, University of Tokyo Report No. 600, 1986.

²²H. de Vries, C. W. de Jager, and C. de Vries, At. Data Nucl. Data Tables **36**, 495 (1987).

²³D. P. Stanley, F. Petrovich, and P. Schwardt, Phys. Rev. C **22**, 1357 (1980).

²⁴J. W. Negele, Phys. Rev. C **1**, 1260 (1970).

²⁵M. Kamimura, Nucl. Phys. **A351**, 456 (1981).

²⁶G. C. Morrison, *Saclay Heavy-ion Conference* [J. Phys. (Paris) **C6**, (1971)] J. L. C. Ford, Jr., K. S. Toth, G. R. Satchler, D. C. Hensley, L. W. Owen, R. M. DeVries, R. M. Gaedke, P. J. Riley, and S. T. Thornton, Phys. Rev. C **10**, 1429 (1974).

²⁷Y. Sakuragi, private communication.